



Review

Copper-containing spherical mesoporous silicates prepared by template-ion exchange: A multitechnique characterization and oxidation properties

Corina M. Chanquía ^{a,e}, Analía L. Cánepa ^{a,e}, Julián Bazán-Aguirre ^a, Karim Sapag ^{b,e}, Enrique Rodríguez-Castellón ^c, Patricio Reyes ^d, Eduardo R. Herrero ^a, Sandra G. Casuscelli ^{a,e}, Griselda A. Eimer ^{a,e,*}

^a Centro de Investigación y Tecnología Química (CITEQ), Universidad Tecnológica Nacional – Facultad Regional Córdoba, Córdoba 5016, Argentina

^b Instituto de Física Aplicada (INFAP), CONICET, Laboratorio de Ciencias de Superficies y Medios Porosos (LaCSuMP), Departamento de Física, Universidad Nacional de San Luis, San Luis 5700, Argentina

^c Departamento de Química Inorgánica, Facultad de Ciencias, Universidad de Málaga, 29071 Málaga, Spain

^d Facultad de Ciencias Químicas, Universidad de Concepción, Casilla 3-C Concepción, Chile

^e CONICET, Avenida Rivadavia 1917, C1033AAJ Buenos Aires, Argentina

ARTICLE INFO

Article history:

Received 18 February 2011

Received in revised form 1 July 2011

Accepted 1 July 2011

Available online 8 July 2011

Keywords:

Copper

Nano-species

Template-ion exchange

M41S

Oxidation test

ABSTRACT

M41S type mesoporous silicate particles with spherical morphology containing copper nano-species were successfully synthesized by the template-ion exchange (TIE) method and compared with those synthesized by the direct hydrothermal (DHT) method. Various techniques including XRD, AAS, adsorption/desorption of N₂, SEM, TEM, TGA, UV–Vis-DRS, TPR, XPS and FT-IR-Py, were employed for the nanocatalysts characterization. A narrow distribution of silicate particle size between 2 and 3 μm, and a primary mesoporosity were evidenced by electronic microscopy, even for loadings of copper of about 7 wt.%. All the materials exhibited a good structural regularity, besides of high surface areas (>1000 m²/g) and pore volumes (~1 cm³/g). A secondary mesoporosity, likely caused by the hydrothermal treatment during the TIE process, was also detected. This new synthesis method showed the advantage of promoting the introduction of copper nano-species to the mesostructure (isolated Cu^{δ+} species and [Cu^{δ+}...O^{δ-}...Cu^{δ+}]_n clusters), minimizing the bulk CuO formation. The coexistence of both oxidation states 1+ and 2+ (δ+) in the major copper species present in these catalysts could be inferred. In addition, all of the samples only showed Lewis acid sites. The cyclohexene oxidation with H₂O₂ has been studied as a catalytic test: the highly dispersed Cu^{δ+} species on the mesopore walls, obtained by TIE method, have been suggested as the main active sites for the oxidation. The allylic oxidation has mainly taken place, with the formation of 2-cyclohexen-1-one and 2-cyclohexen-1-ol as major products.

© 2011 Elsevier Inc. All rights reserved.

Contents

| | |
|--|----|
| 1. Introduction | 3 |
| 2. Experimental methods | 3 |
| 2.1. Catalyst preparation | 3 |
| 2.2. Characterization techniques | 4 |
| 2.3. Catalytic test | 4 |
| 3. Results and discussion | 4 |
| 4. Conclusions | 11 |
| Acknowledgments | 11 |
| References | 11 |

* Corresponding author at: Centro de Investigación y Tecnología Química (CITEQ), Universidad Tecnológica Nacional – Facultad Regional Córdoba, Córdoba 5016, Argentina. Tel./fax: +54 351 469058.

E-mail addresses: cchanquia@scdt.frc.utn.edu.ar (C.M. Chanquía), geimer@scdt.frc.utn.edu.ar (G.A. Eimer).

1. Introduction

The use of supramolecular assemblies, such as surfactant micellar aggregates, as structure directing agents in soft chemistry based silica gelation processes resulted in the discovery of a new family of mesoporous silica compounds called M41S [1–4]. In particular, MCM-41 is one of the most attractive porous materials because of its characteristic structure of well-ordered hexagonal mesopores [2,3]. The large surface area ($\sim 1000 \text{ m}^2/\text{g}$) and the uniform mesopores with controllable diameter of 2–10 nm have made these nanostructured materials highly desirable in various fields such as nanocatalysis. However, siliceous mesoporous materials do not have sufficient intrinsic activities as catalysts, and thus several methods have been developed for introducing catalytically active sites such as metals, metal ions and metal complexes into mesoporous silica [5,6]. In this context, the soft chemistry based processes (i.e. chemistry at low temperatures and pressures, from molecular or colloidal precursors) clearly offer innovative strategies to obtain tailored nanostructured materials. The mild conditions of sol–gel chemistry provide reacting systems mostly under kinetic control. Therefore, slight changes of experimental parameters (i.e., pH, concentrations, temperatures, nature of the solvent, and counterions) can lead to substantial modifications of the resulting supramolecular assemblies and give rise to solids with very different structures and properties [7,8]. The most extensively studied method for the introduction of active sites is the direct hydrothermal (DHT) method, i.e. directly adding the metal ion precursors to the synthesis gel before hydrothermal synthesis. Different from aluminosilicate zeolites, the purely siliceous mesoporous materials do not possess ion exchange ability. However, it has been found that metal ions can also be implanted into MCM-41 by exchanging the template cations embedded in the channels of the as-synthesized MCM-41 with the metal ions in solution [9–11]. Thus, the cationic surfactants in the as-synthesized MCM-41 can be replaced through template-ion exchange (TIE) by other positively charged cations. It can be expected that different synthetic methods would result in different environments of the active sites introduced to MCM-41, which may behave differently in catalytic reactions. Thus, the elucidation of the structure–property relationship of the metal ion incorporated to MCM-41 is crucial for the catalytic applications of these materials. Takehira et al. have applied two different methods, i.e., direct hydrothermal synthesis (DHT) and template-ion exchange (TIE), to the syntheses of V-, Fe-, Cr- and Mn-MCM-41 [12–19]. The two methods resulted in different locations and coordination environments of the incorporated metal cations; the TIE method provided highly dispersed metal ions on the wall surface of MCM-41 inside the mesopores and the DHT method tends to incorporate metal ions inside the framework of MCM-41. It has been clarified that the two different methods for introducing metal ions bring about remarkably different catalytic behaviors. Thus, Liu and Teng employed the TIE method to prepare copper supported on MCM-41 and examined the influence of metal introducing technique on the NO reduction [11]. Recently, Ikeda et al. reported the reaction of ethene to propene catalyzed on Ni-M41S prepared by the TIE method [20].

The use of nanocatalysts such as transition metals-modified M41S type molecular sieves emerged as an interesting option for the development of environment compatible processes, substituting the homogeneous catalysis. In particular, in the field of fine chemical, the selective oxidation of olefinic compounds plays one of the important roles in the synthesis of organic compounds of high added value [16]. The diluted hydrogen peroxide (H_2O_2) is one of the most convenient oxidants in use due to its easy manip-

ulation, high active oxygen content and the absence of byproducts [21]. There are numerous reports about the application of mesoporous catalysts modified with Ti and V by DHT in olefins oxidation processes with H_2O_2 , showing high conversion levels [22–24]. However, mesoporous materials modified with Cu have not been almost evaluated in this process [25], despite the same are very promising candidates due to its special redox properties, polarizability and particularly lower cost [26–28]. Among the studied olefins, the cyclohexene is generally used to evaluate the redox ability of modified MCM-41 using H_2O_2 as oxidant [22,23,29,30]. At the moment, we have found very few reports about the cyclohexene oxidation using mesoporous materials modified with Cu and no reports using the TIE method. In particular, Malumbazo and Mapolie [31] informed complexes of Cu (II) immobilized on MCM-41 for this reaction using H_2O_2 as an oxidant ($\text{C}_6\text{H}_{10}/\text{H}_2\text{O}_2$ molar ratio = 1/1) and molecular oxygen as a co-oxidant at 60 °C. Allylic species were isolated as the major products with a C_6H_{10} conversion of about 45%.

In this work the physicochemical properties of the Cu-containing mesoporous molecular sieves M41S type, synthesized by the TIE method, were carefully studied and compared with those of the materials synthesized by the DHT method, reported by us elsewhere [32,33]. The selective oxidation of cyclohexene with H_2O_2 was studied as a catalytic test for both synthesis methods.

2. Experimental methods

2.1. Catalyst preparation

The parent siliceous mesoporous molecular sieve (Si-MMS) was synthesized using cetyltrimethyl ammonium bromide (CTABr, Aldrich) as template and tetraethoxysilane (TEOS, Fluka > 98%) as Si source. In a typical synthesis, TEOS, 25 wt.% solution of CTABr in ethanol and 70% of the tetraethylammonium hydroxide 20 wt.% aqueous solution (TEAOH, Sigma–Aldrich) were added dropwise and stirring was continued during 3 h. Finally, the remaining TEAOH and the water were further added dropwise to the milky solution which was then heated at 80 °C for 30 min to remove ethanol used in solution and produced in the hydrolysis of TEOS. The pH of the resultant gel was 13. The molar composition of initial gel was: TEAOH/Si = 0.3; CTABr/Si = 0.3; $\text{H}_2\text{O}/\text{Si} = 60$. The white solid product formed during the synthesis process, without any further treatment, was filtered, washed with distilled water until pH ~ 7 and dried at 60 °C overnight to give the as-synthesized Si-MMS. This consisted, according to the thermogravimetric analysis, of ~ 40 wt.% of SiO_2 and ~ 60 wt.% of surfactant. For the preparing of the mesoporous molecular sieves modified with copper (Cu-MMS) by using the template ion exchange (TIE) method, 1.85 g of the as-synthesized Si-MMS was vigorously stirred in 38 mL of a $\text{Cu}(-\text{NO}_3)_2 \cdot 3\text{H}_2\text{O}$ (Anedra) aqueous solution with different concentrations (2.77×10^{-3} to 1.6×10^{-2} M) at ambient temperature for 1 h. This mixture was placed into a Teflon-lined stainless-steel autoclave and hydrothermally treated in an oven at 80 °C for 1 day under autogeneous pressure. The resulting light blue solid was then filtered, washed and dried at 60 °C overnight. The template was evacuated from the Cu-MMS as-synthesized samples by heating (2 °C/min) under air flow (45 mL/min) at 550 °C and calcined at the same temperature for 6 h. The final colour of the calcined samples was brown, which turns to beige for the solid with the lower copper content. These copper-modified catalysts were named as Cu-M(x), where x indicates the copper content in wt.% in the final solids.

2.2. Characterization techniques

The materials were characterized by powder X-ray diffraction (XRD), nitrogen adsorption/desorption, scanning electronic microscopy (SEM), transmission electronic microscopy (TEM), thermogravimetric analysis (TGA), UV–Vis diffuse reflectance (UV–Vis-DRS) spectroscopy, temperature-programmed reduction (TPR), X-ray photoelectron spectroscopy (XPS) and Fourier transform infrared spectroscopy with pyridine adsorption (FT-IR-Py). The Cu content in the final solid products was determined by atomic absorption spectroscopy (AAS) using an AA Varian Spectra spectrophotometer. The samples were previously digested using HF and HNO₃ in a 2:1 ratio, and then were diluted with distilled water until 4.5 mL of solution. The percent relative uncertainty of the AAS results was 5%. XRD patterns were collected in air at room temperature on a Philips PW 1729 diffractometer using CuK_α radiation of wavelength 0.15418 nm. Diffraction data were recorded in the $2\theta = 1\text{--}8^\circ/34\text{--}40^\circ$ ranges at an interval of 0.02° and a scanning speed of $0.3^\circ/\text{min}$ was used. The mean crystalline sizes of the CuO oxides were calculated by applying Scherrer equation using the FWHM (full width at half maximum) values of the most intense peaks. The specific surface area, the pore size distribution and the total pore volume were determined from the N₂ adsorption/desorption isotherms obtained at -196°C using a Micromeritics ASAP 2010. The surface area was determined by the Brunauer, Emmett and Teller (BET) method using the range of P/P_0 points between 0.05–0.15 for the Si-MMS parent, and 0.05–0.23 for the Cu-M(x) catalysts. The pore size was calculated by the Barrett, Joyner and Halenda (BJH) method, based on the Kelvin equation and obtained for the adsorption branch. The primary mesoporous volume was estimated by the alpha plot method, the total pore volume by the Gurvich rule at $P/P_0 \sim 0.98$, and the secondary mesoporous volume by the difference. SEM micrographs were obtained in a JEOL model JSM 6380 LV. lower resolution TEM images were obtained in a Jeol Model JEM-1200 EXII System. Thermogravimetric analysis was performed in Shimadzu TGA-51 in the following conditions: air flow of 50 mL/min with heating rate of $10^\circ\text{C}/\text{min}$. UV–Vis-DR spectra of the materials were recorded using a Perkin Elmer precisely – Lambda 35 spectrophotometer, to which a diffuse reflectance chamber Labsphere RSA-PE-20 with an integrating sphere of 50 mm diameter and internal Spectralon coating is attached. Once the solid samples were compacted in a Teflon sample holder to obtain a sample thickness of ~ 2 mm, their spectra were recorded at 100 nm/min in the range 200–900 nm. Spectral grade BaSO₄ was used as the reference material. The spectra were taken in air at room temperature and the data were automatically transferred according to the Kubelka–Munk equation: $f(R) = (1 - R_\infty)^2 / 2R_\infty$. The original spectra obtained for the calcined samples were fitted by three bands using the NLSF (Nonlinear Least Squares Fitter) Wizard of OriginPro 7.5 software. Curve-fitting calculations were useful for determining the location of the bands and their areas; the fitting confidence was $\chi^2 \leq 0.0005$ and $R^2 \geq 0.999$. The reducibility of the calcined copper catalysts was measured by the TPR experiments in the Micromeritics 2900 equipment. In these experiments, the samples were heated at a rate of $10^\circ\text{C}/\text{min}$ in the presence of H₂ (5% H₂/Ar flow, 20 mL/min STP) and the reduction reactions were monitored by the H₂ consumption. X-ray photoelectron spectra were collected using a Physical Electronics PHI 5700 spectrometer with non-monochromatic Mg K_α radiation (300 W, 15 kV, 1253.6 eV) for the analysis of photo-electronic signals of C 1s, O 1s, Si 2p and Cu 2p and multichannel detector. Spectra of powdered samples were recorded with the constant pass energy values at 29.35 eV, using a 720 μm diameter analysis area. During data processing of the XPS spectra, binding energy values were referenced to the C 1s peak (284.8 eV) from the adventitious contamination layer. A short acquisition time of 10 min was

used to examine C 1s, Cu 2p and CuLMM XPS regions in order to avoid, as much as possible, photo-reduction of Cu(II) species. The PHI ACCeSS ESCA-V6.0 F software package was used for acquisition and data analysis. A Shirley-type background was subtracted from the signals. Recorded spectra were always fitted using Gauss–Lorentz curves, in order to determine the binding energy of the different element core levels more accurately. The error in the BE was estimated to be ca. ± 0.1 eV. FT-IR spectral measurements of pyridine adsorption on the samples were performed on a JASCO FT-IR 5300 spectrometer equipped with DTGS detector. The range and resolution of acquisition were 4600–400 and 4 cm^{-1} , respectively. A self-supporting wafer for each sample (~ 20 mg and 13 mm of diameter) was prepared, placed in a thermostated cell with CaF₂ windows connected to a vacuum line and evacuated for 8 h at 400°C . The background spectrum was recorded first after cooling the sample to room temperature. Afterwards, the solid wafer was exposed to pyridine vapors (Sintorgan, 99% purity) until saturate the system to ~ 46 mm Hg at room temperature; the contact time at this pressure was 12 h. The IR spectrum for each sample was obtained after pyridine desorption by evacuation for 1 h at 100 and 200°C . All the spectra were recorded at room temperature before and after pyridine adsorption and desorption at each temperature. The difference spectrum was obtained finally by subtracting the background spectrum recorded previously.

2.3. Catalytic test

The cyclohexene oxidation reactions with H₂O₂ were performed at 70°C under vigorous stirring in 2 mL glass vials placed in a temperature controlled water bath. Typically, the reaction mixture for each vial consisted of 91.9 mg of cyclohexene (Baker, 98%), 26.60 mg of hydrogen peroxide (35 wt.%, Riedel-de Haën), 678.30 mg of acetonitrile (Sintorgan, 99.5%) and 9.00 mg of nanocatalyst. The vials were withdraw at different sampling times, the aliquots were filtered and analyzed by gas chromatography (Hewlett Packard 5890 Series II) using a capillary column (cross-linked methyl-silicone gum of $30\text{ m} \times 0.53\text{ mm} \times 2.65\text{ mm}$ film thickness) and a flame ionization detector. Additionally, reaction products were identified by mass spectrometry (Shimadzu GC-MS QP 5050) with HP-5 capillary column. The total conversion of H₂O₂ was measured by iodometric titration. The H₂O₂ efficiency was calculated as the percentage of this reactive converted to oxidized products. Also it was calculated the ratio of cyclohexene conversion to theoretically possible conversion (mol% of max.) and the selectivity as (mol product/total mol products) $\times 100$. The relative uncertainties of the measurements were tested with repeated determinations. The percent relative uncertainty (CV (%)) of the result was calculated by dividing the corresponding absolute uncertainty with the average of the measurements.

3. Results and discussion

The XRD patterns of the calcined Cu-MMS prepared by the TIE method with different copper contents, together with the corresponding calcined parent Si-MMS sample are shown in Fig. 1. The Cu-MMS materials exhibit an intense low-angle reflection between 1.5° and 3.5° , besides a weak reflection between 3.5° and 5.5° characteristic of mesoporous materials M41s type, which remained stable under calcination. In contrast to that reported by Gac et al. [34], the Cu-MMS synthesized by using the TIE method exhibit better structural regularity than his parent Si-MMS. Thus, the hydrothermal treatment involved in the TIE procedure is likely to improve the structure of the Cu-MMS. On the other hand, in concordance to what is said by some authors the heteroatom content increasing in the synthesis mixture did not affect substantially the

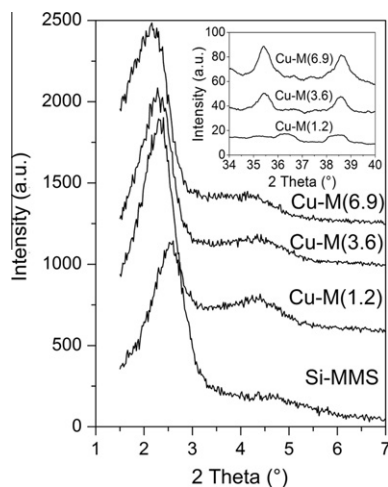


Fig. 1. XRD patterns of the samples prepared with different copper contents.

ordering of the materials synthesized by the TIE method [9,11,15,19]. It is noteworthy that, even for a copper content around ~7 wt.%, a good structural regularity was obtained. Finally, as the content of Cu is increased, the main peak shifted toward lower diffraction angles, which will be consistent with a probable incorporation of Cu into the siliceous structure [16,22,29,35].

The high angle XRD results in the region between 34° and 40° are shown as the inset in Fig. 1. Cu-M(6.9) and Cu-M(3.6) samples exhibit two peaks at 35.6° and 38.8° typical of the CuO phase [26,36–39]. Nevertheless, very weak and broad reflections were observed, which are characteristic of very small CuO particles. An approximate estimation of the CuO particle dimensions, performed from the broadening of the peak at $2\theta = 35.6^\circ$ by the Scherrer formula [40], had values in the range between 17 and 26 nm. As it can be observed through the relative areas of the peaks, a more concentrated $\text{Cu}(\text{NO}_3)_2 \cdot 3\text{H}_2\text{O}$ solution favors the formation of CuO oxide particles on the surface of the solid. It should be noted here that for the Cu-M(1.2) sample the signal/noise ratio is enough low and therefore no peak can be considered in its XRD pattern. Finally, diffraction peaks corresponding to the Cu_2O phase ($2\theta = 36.44^\circ$ and 42.33°) and the Cu^0 phase ($2\theta = 43.3^\circ$ and 50.5°), could not be observed for the Cu-MMS catalysts.

Fig. 2 shows the N_2 adsorption/desorption isotherms (a) with their corresponding pore size distribution (b) of the calcined Cu-MMS and Si-MMS samples; the corresponding physical parameters are collected in Table 1. It must be noted that for comparisons of different samples the curves have been shifted in the y-axis. All of the samples exhibit type IV isotherms typical of mesoporous structures with an inflection at relative pressure $P/P_0 \sim 0.2$ – 0.4 characteristic of capillary condensation inside the conventional mesopores present in MCM-41 structure (primary or structural mesopores) [41]. Such inflection provides a measure of the distribution range of the pore size of these materials [42]. The adsorption isotherms for the Cu-M(1.2) and Cu-M(3.6) samples featured a narrow step of capillary condensation, which provides clear evidence of their narrowly defined pore diameter range; meanwhile the adsorption isotherms of the Si-MMS and Cu-M(6.9) samples exhibited a slightly more broad capillary condensation step, which indicates a bigger range in the distribution of the pore size [42]. Such feature is also evidenced by the low intensity and larger width of the peaks in the pore size distribution curve showed in Fig. 2(b). In addition, the position of the capillary condensation step gradually shifted from the relative pressure of about 0.24 for the parent Si-MMS sample to about 0.3 for the Cu-M(6.9) sample. This gradual change indicates an increase in the pore size (Table 1),

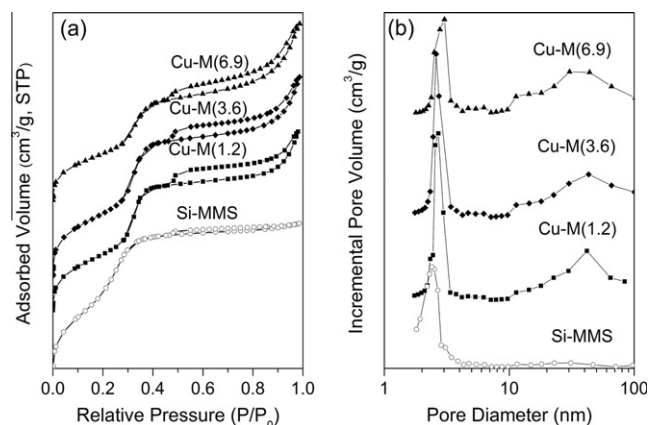


Fig. 2. N_2 adsorption/desorption isotherms and pore size distribution of the samples prepared with different copper contents.

Table 1

Structural parameters of the catalysts synthesized with different copper contents.

| Sample | $D_{\text{BJH}}^{\text{a}}$ (nm) | $V_{\text{pores}}^{\text{b}}$ (cm^3/g) | | $S_{\text{BET}}^{\text{c}}$ (m^2/g) |
|-----------|----------------------------------|--|-----------|---|
| | | Primary | Secondary | |
| Si-MMS | 2.39 | 0.98 | 0.14 | 1520 |
| Cu-M(1.2) | 2.74 | 0.82 | 0.42 | 1155 |
| Cu-M(3.6) | 2.68 | 0.84 | 0.57 | 1250 |
| Cu-M(6.9) | 2.71 | 0.55 | 0.72 | 1000 |

^a BJH pore diameter.

^b Pore volume.

^c BET specific surface area.

which can also be expected on the basis of the systematic changes in the unit cell parameter for the samples [43]. On the other hand, the Cu-MMS samples exhibited a pronounced increase in the adsorption branch at relative pressures about 0.85, which could be due to a capillary condensation in secondary mesopores [28,44]; in regard to this, the Fig. 2(b) shows a broad peak between 20 and 100 nm in the distribution of pore size, which could be attributed to this secondary mesoporosity. Furthermore, hysteresis loops that resemble H4-type with a sharp decrease in the desorption branch at $P/P_0 \sim 0.45$ – 0.5 , evidence the existence of ink-bottle pores [45]. The secondary mesopore volume for all the samples is shown in Table 1. This non-structural porosity will be consisting of large cavities eventually interconnected and accessible through necks, which have an average diameter smaller than those of the main voids. It is noteworthy that the parent Si-MMS sample synthesized without any treatment does not exhibit secondary mesopores. Therefore, it might be inferred that the hydrothermal treatment employed in the TIE method promotes the formation of this secondary mesoporosity, possibly from the rupture of thin pore walls by the direct attack of water molecules to the silica surface when the template is exchanged. Finally, we suggest that the formation of this secondary mesoporosity may favor the diffusion of copper species into the internal surface of the molecular sieve and therefore the template-ion exchange process during the hydrothermal treatment.

As it can be observed in Table 1, all of the samples show surface areas above $1000 \text{ m}^2/\text{g}$ and total pore volume above $1 \text{ cm}^3/\text{g}$, which are typical of mesoporous materials. Even though the Cu-MMS showed higher structural regularity than the parent Si-MMS material, those samples presented lower specific surface areas. Four causes may be giving account for this surface area reduction: (1) the intrapore formation of enough small CuO nano-particles (no detectable by XRD) and/ or $[\text{Cu}^{\delta+} \dots \text{O}^{\delta-} \dots \text{Cu}^{\delta+}]_n$

clusters finely dispersed within the mesopores; (2) the blocking of pores of the meso-structure by bulky CuO oxides; (3) the introduction of Cu^{δ+} ions into the M41S framework which leads to an increase in density of the composites; (4) the building-up of the secondary mesoporosity.

The particle size and morphology of the Cu-MMS were investigated by scanning electron microscopy. The SEM images of the representative Cu-M(3.6) sample are presented in Fig. 3. As it can be seen, these materials show spherical-like morphology in the micrometer-range with a narrow particle-size distribution in the range between 2 and 3 μm. It is noteworthy that although there are fragments of material between the Cu modified silica spheres, its proportion is lower than that found in the samples synthesized by direct hydrothermal treatment (DHT) [33]. This is probably possible due to that the pure siliceous spheres were firstly built without any thermal treatment [46]. Then, a little amount of fragments could be generated from the building-up of the secondary mesoporosity during the hydrothermal treatment employed by the TIE method.

Measurements of transmission electron microscopy of the Cu-MMS were made in order to examine their structural regularity and elucidate the nature of the nonstructural porosity. Fig. 4 show TEM images of the sample Cu-M(6.9), taken as representative. As it can be observed in the (a) and (b) micrographs, regions of low contrast randomly interrupt the pores arrangement characteristic of the mesoporous materials. Such weak regions can be attributed to the presence of cavities that permeate the entire bulk, giving rise to the spongelike porosity or secondary mesoporosity mentioned above [44]. The existence of a spongelike porous network might have relevance for catalysis, as it would probably enhance the diffusion of reactants through the particles. On the other hand, as shown in the images (b) and (c), these materials present a primary mesoporous structure although a two-dimensional hexagonal ordering of pores characteristic of MCM-41 materials has not been observed. Finally, these micrographs also present some high-contrast regions which would be attributed to CuO nano-particles. In concordance with the XRD measurements, the images (a) and (b) reveals a particle diameter for these nano-oxides of around ~30 nm. Since the TIE technique is a “quasi” post-synthesis method to introduce metals into the silica, we expect that the nano-particles of CuO grow on the external surface of the silicate. However, it is not possible to exclude the possibility that some nano-oxides are located inside the sponge-like porosity, although more easily accessible than in the case of the samples prepared by DHT, as show image (a) [33].

In order to understand the template-ion exchange process, a thermogravimetric analysis in the parent Si-MMS and Cu-M(3.6) as-synthesized samples was performed. The results of this analysis are shown in the Fig. 5. As it can be observed, for both samples, the removal process is complex and involves several steps. The weight

loss of ~5% below 150 °C corresponds to desorption of physisorbed water [47,48]. According to the literature [49,50], the weight loss between 150 and 250 °C would be caused by the elimination of the amines head groups via Hofmann degradation and evaporation of alkenes resulting from this degradation. The weight change in the 250–300 °C temperature range has been attributed to successive carbon chains fragmentation or decomposition, with early oxidation of organic fragments. Finally, the oxidation of the remaining organic components towards carbon dioxide and water occurs between 300 and 400 °C; some water can also be produced from condensation of Si–OH groups at the silica surface beyond 350 °C [47–49]. For Si-MMS and Cu-M(3.6) samples, the weight loss between 150 and 800 °C, corresponding to the surfactant, is ~58% and ~42%, respectively. These results suggest that during the hydrothermal treatment employed in the TIE process, a surfactant proportion (~16%) get out from the pores of parent Si-MMS towards the reaction medium. This would favor the copper species diffusion inside of the pores in the cationic exchange process.

The UV–Vis–DR spectra were recorded in order to understand the coordination environment of Cu species. These spectra for the calcined samples prepared with different copper contents are shown in Fig. 6. The Si/Cu atomic ratio and the overall metal content in the final solid as well as the relative distribution of copper species, determined by UV–Vis–DR, are presented in Table 2. The original spectra have been decomposed into three contributions to facilitate the assignment to the different Cu species. According to a detailed study about the UV–Vis–DR spectra of Cu-MMS reported by us elsewhere, these bands can be assigned to the following copper species [32,50–59]: (1) isolated mononuclear Cu^{δ+} cations possibly in coordination with lattice oxygen, related to the sub-band between 250 and 400 nm; (2) linear oligonuclear [Cu^{δ+}...O^{δ-}...Cu^{δ+}]_n clusters like chains possibly inserted into mesoporous channels, related to the sub-band between 400 and 600 nm; (3) bulky CuO oxides segregated of the siliceous structure, related to the sub-band between 600 and 800 nm.

In order to obtain a rough estimation of the wt.% of the different Cu species in the samples, the percentage of each sub-band area with respect to the total area of the experimental spectrum has been multiplied with the overall Cu content (accurately determined by AAS) (see Table 2). Being aware that the obtained values in Table 2 are inaccurate to a certain degree due to the deconvolution procedure, they are nevertheless regarded to be helpful for a comparison of different samples [60]. Unlike the samples prepared by DHT [32], where an increase in the copper content in the initial gel promotes the generation of larger CuO particles, the relative distribution of copper species in the samples synthesized by the TIE method is independent of copper content employed for its synthesis. Judging by the relative percentage of their sub-band areas, the mononuclear Cu^{δ+} ions and the oligonuclears [Cu^{δ+}...O^{δ-}...Cu^{δ+}]_n clusters play a dominant role in these Cu-MMS catalysts. Finally, it should to be noted that this last

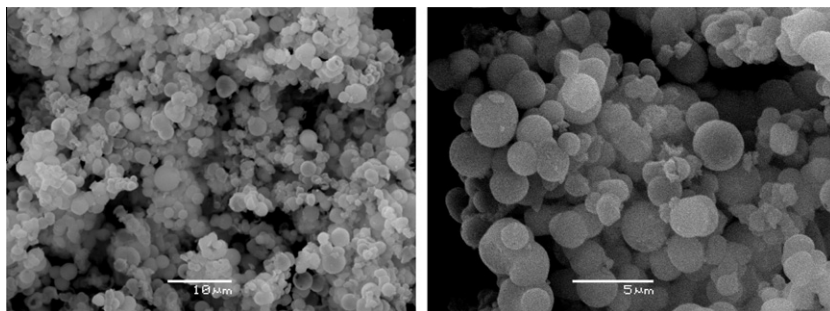


Fig. 3. Scanning electron micrographs of the the Cu-M(3.6) sample.

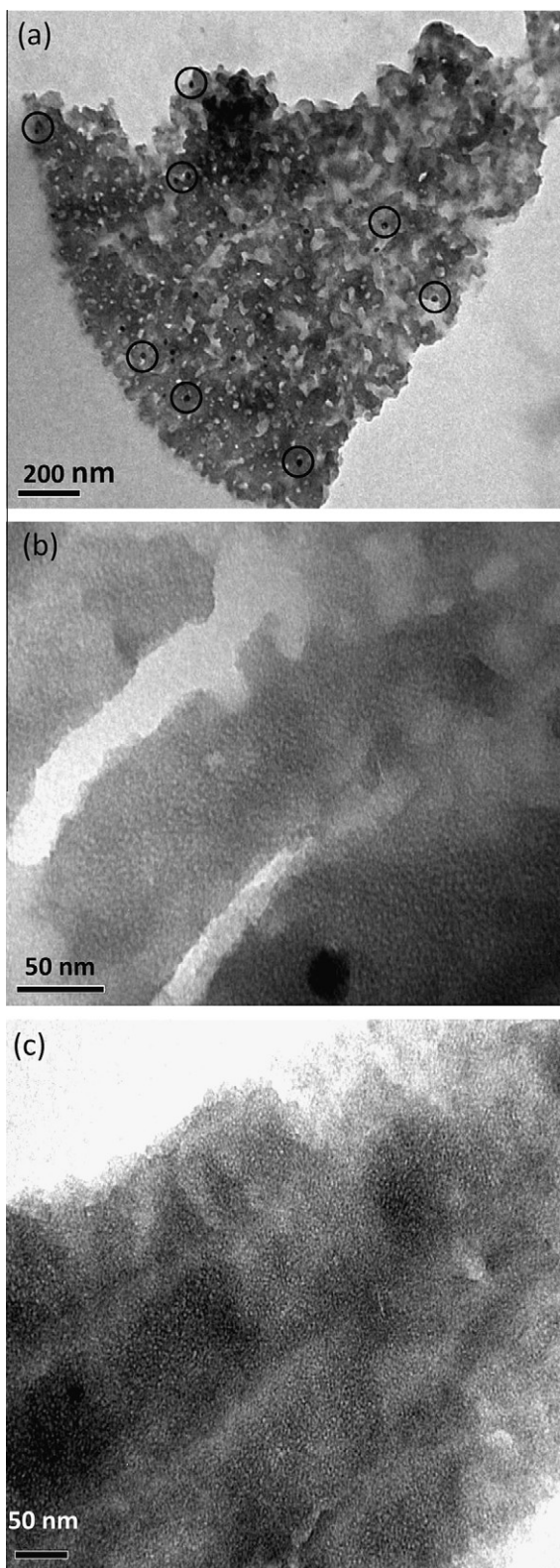


Fig. 4. Transmission electron microscopy images of Cu-M(6.9) sample.

specie could not be detected by TEM, probably due to its very small size and the low resolution of the measuring equipment.

The reducibility of the copper species in the Cu-MMS was investigated by temperature programmed reduction (TPR) experiments and the corresponding profiles are displayed in the Fig. 7. This

figure shows the normalized H₂ consumption curves, obtained by dividing the H₂ consumption signal by the amount of catalyst employed in the experiments. Many authors informed that the segregated CuO would be reduced to Cu⁰ by H₂ in one step at about ~310 °C [35,61,62] and that the values of the temperature maximum and the peak width increase with increasing CuO particle size [62,63]. As it can be seen in Fig. 7, all of the samples exhibit a reduction peak centered at about 290 °C, which is assigned to the reduction of very small CuO nano-particles and/or [Cu^{δ+}...O^{δ-}...Cu^{δ+}]_n nano-clusters inserted in the pores [32], and whose intensity increases with increasing copper content. In comparison to the samples synthesized by DHT [32], these materials did not show any peak around ~350 °C corresponding to larger CuO particles. Finally, it could be said that the lack of reduction peaks at higher temperatures (>400 °C) confirms the strong interaction of isolated Cu^{δ+} species with the framework.

Usually, XPS is a powerful technique at superficial level to explore the oxidation state of the transition metal compounds with localized valence *d* orbitals, due to the different energies of the photoelectrons [64–66]. The Cu²⁺ has mainly *d*⁹ character, while the Cu⁺ is expected to have a full 3*d* shell. The Cu 2*p* core level spectra of the samples prepared with different Cu contents after 10 min of irradiation are shown in Fig. 8. In addition, Table 3 summarizes the binding energy values, Cu_{sat}/Cu_{2*p*} intensity ratios and surface Si/Cu and O/Si atomic ratios as well as the quantification of both species Cu⁺ and Cu²⁺ considering the Cu 2*p*_{3/2} region, for this samples. The assignment of the signals at the different copper states was already discussed by us elsewhere [32]. Thus, the Cu 2*p* region shows two peaks at 935.1 and at 955.2 eV assigned to the doublet Cu²⁺ 2*p*_{3/2} and 2*p*_{1/2} respectively, along with two shake-up satellite peaks at ~943.2 and ~963.6 eV. It is known that these satellite signals are attributed to an electron transfer from a ligand orbital to a *d* orbital of the metal. This transition is a *np* (ligand) → 3*d* (metal) transition [67], which is impossible for Cu⁺ and Cu⁰ species that have filled *d* levels, but is mainly a characteristic of bivalent copper [66]. In addition, these spectra also exhibited two peaks at ~933 and ~953.4 eV, which are attributable to the doublet Cu 2*p*_{3/2} and Cu 2*p*_{1/2} levels for Cu⁺ species. Moreover, as it can be seen, these peaks are more intense than those corresponding to Cu²⁺ ions. It is necessary to note that the Cu⁺ ion is difficult to distinguish from zero-valence copper by XPS. However, we do not support the existence of zero-valence copper in the catalyst due to the calcination process performed under the air conditions; besides the Cu⁰ signal is not observed in XRD patterns. Therefore, the XPS results showed copper to be present in both the oxidation states Cu⁺ and Cu²⁺, with a slightly higher relative proportion of Cu¹⁺. Moreover, the intensity ratio of the shake-up satellite and the intensity of the Cu 2*p*_{3/2} peak (ICu_{sat}/ICu_{2*p*}) was 0.34 for sample Cu-M(3.6), a far value to that found for CuO (0.55) [68,69]. In addition, the O 1*s* peak position at ~533.2 eV is as expected for silica. Likewise, ~103.8 eV for the Si 2*p* peak is in agreement with SiO₂-type material [70]. The binding energy values of these latter peaks for all of the samples not substantially changed. On the other hand, the surface Si/Cu atomic ratios are rather higher than those obtained from ICP-MS measurements (see Table 2); however, in comparison with the samples prepared by DHT [32], these materials synthesized by the TIE method showed lower surface Si/Cu molar ratios, indicating a higher proportion of copper nano-species on the external surface.

The chemisorption of pyridine followed by IR studies is usually a useful probe to detect the presence and nature of acid sites on a catalyst [29]. Information on the strength of Lewis and Brønsted acid sites can be obtained from pyridine thermodesorption. Fig. 9 shows FT-IR spectra of the calcined samples synthesized by the TIE method with different contents of copper, recorded after the adsorption of pyridine and subsequent evacuation at 100

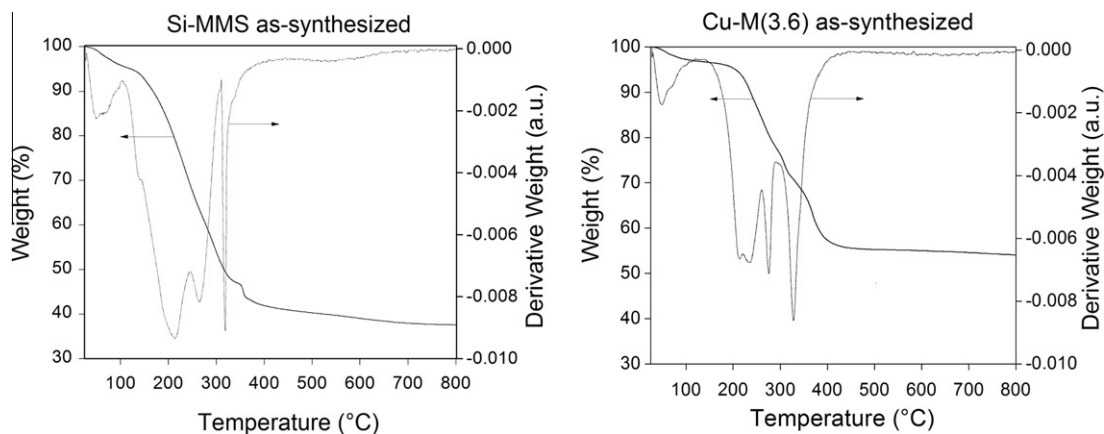


Fig. 5. TGA curves and derivatives of Si-MMS and Cu-M(3.6) as-synthesized samples.

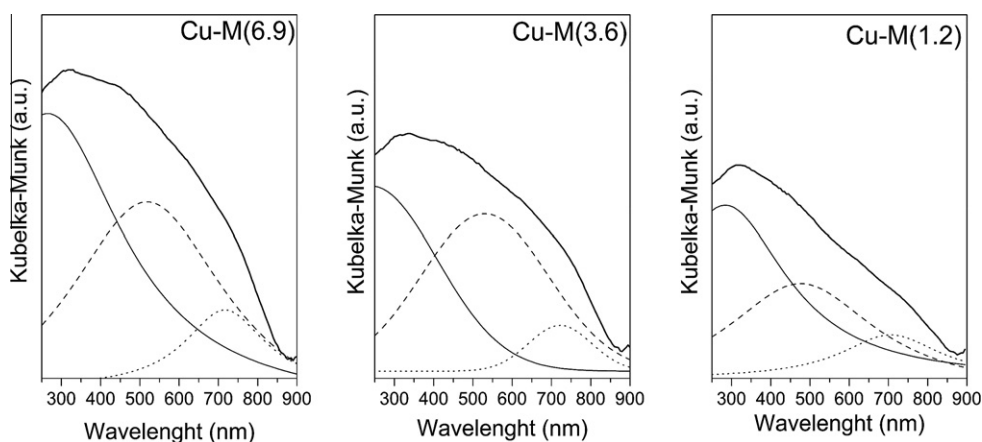


Fig. 6. UV-Vis diffuse reflectance spectra of the samples modified with different copper contents; experimental spectra, thick solid lines; decomposed contributions, thin lines; assignments: – isolated $\text{Cu}^{\delta+}$, – oligomeric $[\text{Cu}^{\delta+}\dots\text{O}^{\delta-}\dots\text{Cu}^{\delta+}]_n$ species, CuO bulky oxides.

Table 2

Chemical composition and copper species relative distribution in Cu-MMS modified with different copper content.

| Sample | Cu cont. ^a (wt.%) | Si/Cu ^a | Distribution of copper species | | | | | |
|-----------|------------------------------|--------------------|--------------------------------|---------|----------|---------|--------|---------|
| | | | Isolated cations | | Clusters | | Oxides | |
| | | | Area% | wt.% Cu | Area% | wt.% Cu | Area% | wt.% Cu |
| Cu-M(1.2) | 1.20 | 87.14 | 50.45 | 0.61 | 39.17 | 0.47 | 10.38 | 0.12 |
| Cu-M(3.6) | 3.60 | 28.69 | 51.52 | 1.85 | 42.38 | 1.53 | 6.10 | 0.22 |
| Cu-M(6.9) | 6.90 | 14.29 | 50.23 | 3.47 | 42.54 | 2.94 | 7.23 | 0.49 |

^a In the final solid.

(curve a) and 200 °C (curve b). All of the samples showed bands corresponding to hydrogen bonded pyridine at 1599 cm^{-1} [71–75], which disappeared upon evacuation at 200 °C. It would indicate a weak interaction between pyridine and the Si–OH groups of the structure. On the other hand, a band at 1608 cm^{-1} , corresponding to pyridine coordinately bonded to Lewis acid sites [71–77] is present in the spectra of all samples. Then, the IR absorption band present at 1448 cm^{-1} can be interpreted in terms of the overlapping of two bands attributed to hydrogen-bonded pyridine and a Lewis-type adduct [76]. Additionally, according to Srinivas et al. [72] the band at 1578 cm^{-1} , present in all of the samples, could be due to pyridine coordinated to weak Lewis acid sites. This band disappears after evacuation at 200 °C. It is noteworthy that the spectra of these catalysts do not show bands at 1540 and 1636 cm^{-1} characteristic of Brønsted acid sites [76,78–80]. Consequently the band at 1485 cm^{-1} , observed in all of the

samples, which is frequently assigned to pyridine interacting with both Brønsted and Lewis acid sites, corresponds only to Lewis acid sites. Finally, according to the presence of their characteristic bands these Lewis acid sites result strong enough to retain the pyridine molecules until 200 °C. Fig. 9 also shows the IR spectra corresponding to the hydroxyl range of the calcined samples before pyridine adsorption. All of the samples present a well-defined band at approximately 3740 cm^{-1} which corresponds to the $\nu(\text{O-H})$ stretching vibrations of hydroxyl groups sitting inside on the wall and outside as terminal OH groups [59,81–85]. Furthermore, a slight shoulder around 3600 cm^{-1} could be indicating the interaction between vicinal OH groups, as Si–OH, Cu–OH and H–OH groups [33]. According to the last results, the clear presence of the terminal Si–OH groups jointly with the scarce broadening between 3700 and 3400 cm^{-1} , allow us to suggest that the isolated $\text{Cu}^{\delta+}$ species would be mainly arising from copper atoms bonded

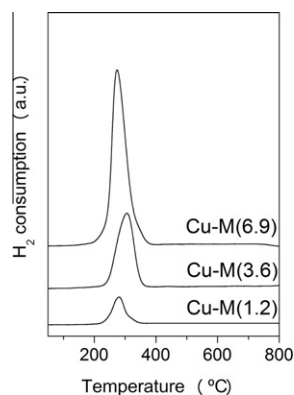


Fig. 7. TPR profiles of the samples modified with different copper contents.

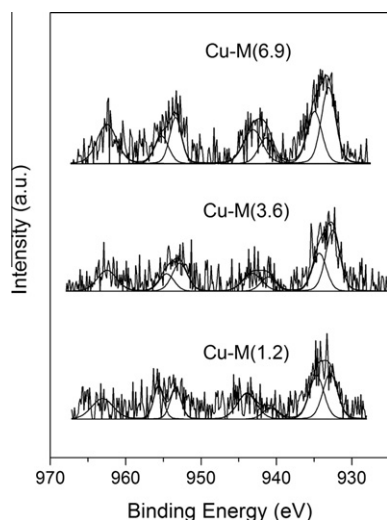


Fig. 8. Cu 2p core level photoelectron profile of the samples modified with different copper contents.

to four framework oxygen atoms [33]. However, the presence of some atoms of copper located in terminal positions as Cu–OH species cannot be discarded [33].

The catalysts synthesized by the TIE method were tested in the reaction of cyclohexene oxidation with H_2O_2 at 70 °C. For comparative purposes, some other reactions were also carried out: without using any catalyst, over Si-MMS itself and over Cu-MMS catalysts synthesized by the DHT method [32,33]. The reaction did not proceed in the absence of the catalyst and the cyclohexene conversion on pure silica Si-MMS was very low (<4 mol% of max.) being the main products cyclohexenol (III) and cyclohexenone (IV). Fig. 10 shows the change of catalytic performances with the copper content over the catalysts synthesized by the TIE and DHT methods. As it can be seen, the materials synthesized by TIE method

showed a medium conversion of cyclohexene despite high consumption of H_2O_2 . The Cu-MMS catalysts synthesized by the DHT method showed low conversion of cyclohexene and moderate consumption of H_2O_2 for the lower Cu contents. The higher cyclohexene oxidation values observed for the materials synthesized by the TIE method compared with those synthesized by DHT method are probably accounting for the presence of highly dispersed $\text{Cu}^{\delta+}$ species on the mesopore walls of M41S structure. Moreover, the cyclohexene conversion is increased when the Cu content increases, which could be mainly related with the increase in the amount of these isolated $\text{Cu}^{\delta+}$ species. In the case of the DHT method, the cyclohexene conversion is lightly decreased with the Cu content increasing which could be attributed to that, although the isolated $\text{Cu}^{\delta+}$ species increase [32], these would be mainly located inside the wall of the mesopores. In order to attempt to confirm that the isolated $\text{Cu}^{\delta+}$ cations are the main active species, the catalytic activity of the samples was again measured after a reduction treatment was performed. The employed reduction conditions (H_2/Ar flow, 20 mL/min; 400 °C) allowed the reduction of both the oligonuclear $[\text{Cu}^{\delta+} \dots \text{O}^{\delta-} \dots \text{Cu}^{\delta+}]_n$ clusters and bulky CuO oxides, as it is inferred of TPR studies (see Fig. 7). Thus, under these conditions, the activity of the materials was not mainly modified. On the other hand, in the present reaction system, the cyclohexene oxidation is accompanied by the side-reaction of self-decomposition of H_2O_2 which proceeds via a sequence of reactions involving free radicals as transient intermediates [86]. The results shown in Fig. 10 combined with the characterization results described above (Table 2 and Fig. 4) allow us to suggest that the $[\text{Cu}^{\delta+} \dots \text{O}^{\delta-} \dots \text{Cu}^{\delta+}]_n$ clusters and the CuO nano-particles, could accelerate the decomposition of H_2O_2 . Then, the high proportion of these species for the material synthesized by DHT method with the highest Cu content would be giving account for the high consumption and the lower efficiency of H_2O_2 (see Fig. 10). Meanwhile, for the catalysts synthesized by TIE method, although the H_2O_2 efficiency increases with the Cu content, the low values observed along with the high H_2O_2 consumption are reflecting the high accessibility of the oxide species despite its low proportion. The main products obtained during cyclohexene oxidation are shown in Scheme 1. In practice, epoxidation and allylic oxidation are often competitive processes in the oxidation of cyclic olefins and frequently both processes occur simultaneously [22]. According to GC–MS analyses, the products mixture is composed of species formed by oxidation of both double bond (cyclohexene oxide (I) and, as byproducts, 1,2-cyclohexanediol (II) and 2-hydroxy-cyclohexanone(VII)) and allylic C–H (2-cyclohexen-1-ol (III), 2-cyclohexen-1-one (IV), 2,3-epoxycyclohexenone (V), 2,3 epoxi-cyclohexen-1-ol (VI)). Fig. 11 presents the selectivity to products as a function of Cu content for both methods, after 5 h. As it is observed, the allylic oxidation has mainly taken place, with the formation of 2-cyclohexen-1-one and 2-cyclohexen-1-ol as major products. A possible mechanism for the cyclohexene oxidation on Cu-MMS involves the interaction between the peroxide and the catalyst, where H_2O_2 is bonded to the isolated $\text{Cu}^{\delta+}$ species. This interaction yields mainly HO \cdot and $\text{HO}_2\cdot$ species via a redox mechanism. Then the HO \cdot radical

Table 3

BE values (in eV), $\text{Cu}_{\text{sat}}/\text{Cu}_{2p}$ intensity ratio and surface Si/Cu and O/Si atomic ratios of the Cu-MMS catalysts.

| Sample | O 1s | Si 2p | Cu 2p _{3/2} | Cu 2p _{1/2} | $\text{ICu}_{\text{sat}}/\text{ICu}_{2p}$ | Si/Cu | O/Si |
|-----------|-------|-------|----------------------|----------------------|---|-------|------|
| Cu-M(1.2) | 533.2 | 103.8 | 932.9 (51%) | 953.0 | 0.39 | 102.4 | 2.0 |
| | | | 934.7 (49%) | 954.7 | | | |
| Cu-M(3.6) | 533.2 | 103.8 | 932.5 (62%) | 952.4 | 0.34 | 80.7 | 2.0 |
| | | | 934.3 (38%) | 954.2 | | | |
| Cu-M(6.9) | 533.2 | 103.9 | 933.1 (59%) | 953.2 | 0.45 | 47.8 | 1.9 |
| | | | 935.5 (41%) | 955.7 | | | |

Note: FWHM values were 2.65 eV for all contributions in Cu 2p spectra. The area ratio of the $\text{Cu}2p_{3/2}/\text{Cu}2p_{1/2}$ doublet was always 2.0.

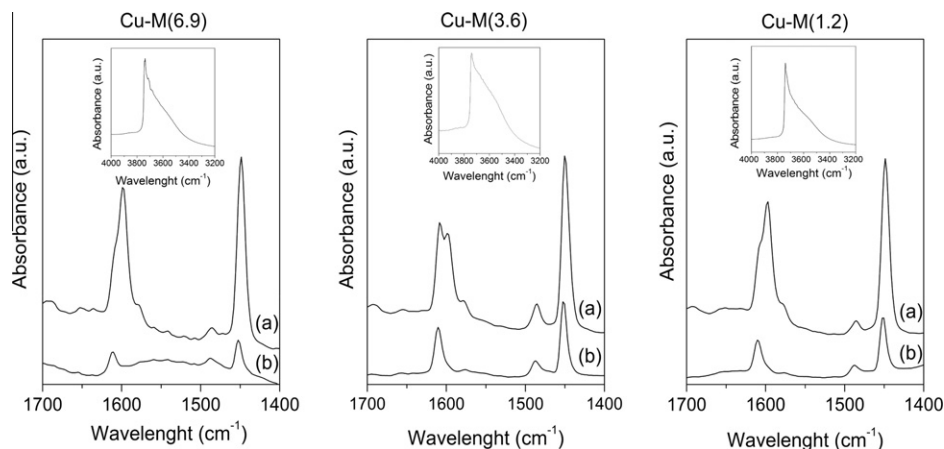


Fig. 9. FTIR of pyridine adsorbed on the samples modified with different copper contents, after desorption at 100 °C (a) and 200 °C (b). Inserted in spectrum of each sample is the region of OH before pyridine adsorption.

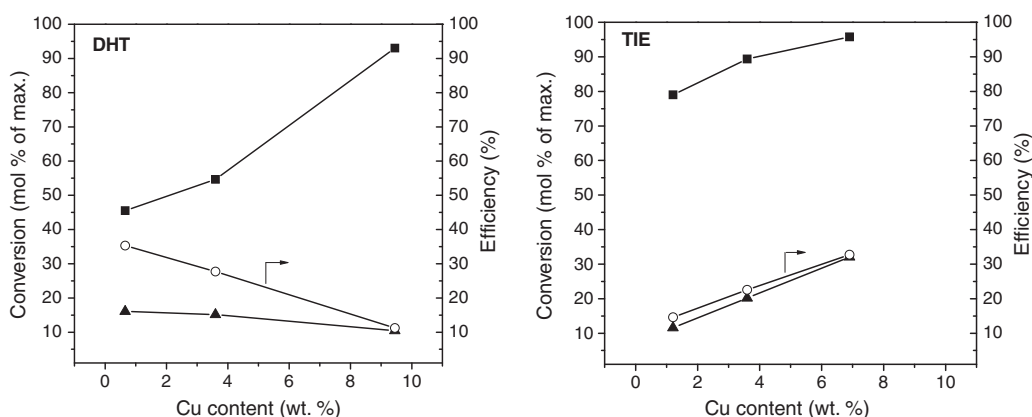
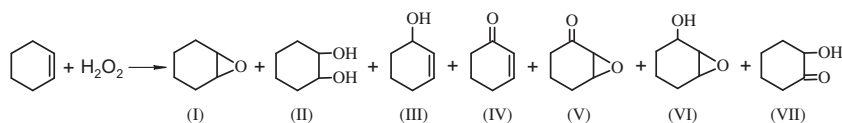


Fig. 10. Effect of Cu content on catalytic results for cyclohexene oxidation with H_2O_2 over Cu-MMS – DHT and TIE. (■) H_2O_2 conversion (%) (CV < 5%), (○) H_2O_2 efficiency (%) (CV < 7%), (▲) Cyclohexene conversion (% of max.) (CV < 7%). Reactions conditions: cyclohexene/ H_2O_2 (mol/mol) = 4/1, Temperature = 70 °C. Catalyst = 9 mg, Reaction time = 5 h.



Scheme 1. Products obtained from cyclohexene oxidation. Epoxidation: cyclohexene oxide (I), 1,2-cyclohexanediol (II) and 2-hydroxycyclohexanone (VII); Allylic oxidation: 2-cyclohexen-1-ol (III), 2-cyclohexen-1-one (IV), 2,3-epoxy-cyclohexanone (V) and 2,3-epoxy-cyclohexen-1-ol (VI).

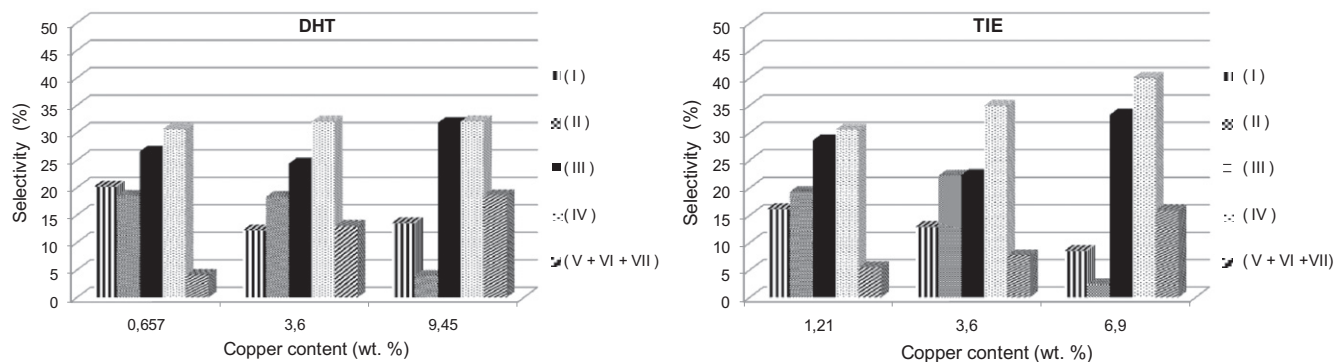


Fig. 11. Influence of Cu content on the selectivity to the cyclohexene oxidation products for both synthesis methods (CV < 5%): (I) cyclohexene oxide, (II) 1,2-cyclohexanediol, (III) 2-cyclohexen-1-ol, (IV) 2-cyclohexen-1-one, (V) 2,3-epoxy-cyclohexanone and (VI) 2,3-epoxy-cyclohexen-1-ol, (VII) 2-hydroxycyclohexanone. Reactions conditions: cyclohexene/ H_2O_2 (mol/mol) = 4/1, Temperature = 70 °C. Catalyst = 9 mg, reaction time = 5 h.

can attack the olefin and yield cyclohexenol and cyclohexenone [86,87].

On the other hand, the observed cyclohexene oxide decreases with the Cu content which is converted to 1,2-cyclohexanediol by the ring cleavage [22,29,88–91]. However it is noticeable that, for the highest Cu contents, this last product decreases whereas the overoxidation products (V + VI + VII) along with allylic alcohol increase. According to literature, the transformation of 1,2-cyclohexanediol could follow two different pathways: a hydration and a dehydrogenation. Thus, the glycol can be dehydrated into the allylic alcohol which could then undergo a further epoxidation of the double bond leading to the formation of overoxidation byproduct (VI). The exact role of whether/how H_2O_2 acts in the dehydration reaction, and how Cu and MCM-41 play a role, remains unclear [92]. It seems probable that the side reactions of epoxide ring cleavage and glycol dehydration proceed on the acid sites of the catalysts. The water present in the reaction medium may compete with the reactant and be adsorbed on the Lewis sites of the catalyst generating Brønsted acid sites which aid this type of reactions [93–95]. On the other hand, the glycol can also be dehydrogenated to the corresponding α -keto-alcohol (VII) [96,97]. However, this reaction, complex in the mechanism, remains under study [98].

Comparing both synthesis methods, although the products distribution is similar, it is possible to observe a slight higher proportion of overoxidation byproducts in the case of the DHT method. This result is probably related with a higher percentage of oxide species.

Finally, it is notable that the catalytic activities reached in this work using the catalysts synthesized by the TIE method are in agreement with those reported by Malumbazo and Mapolie [31]; nevertheless, the cyclohexene oxidation values achieved by these authors were obtained employing molecular oxygen as a co-oxidant.

4. Conclusions

Copper modified mesoporous silicate particles with spherical morphology in the 2–3 μm range, were synthesized by the template-ion exchange method and compared with those synthesized by the DHT method. By analyzing the UV–Vis-DR and XPS techniques, the coexistence of both Cu oxidation states 1+ and 2+ (δ^+) could be inferred. It has been found that the hydrothermal treatment employed in the TIE method developed by us, besides to promoting the introduction of copper nano-species to the mesostructure (isolated $Cu^{\delta+}$ species and $[Cu^{\delta+} \dots O^{\delta-} \dots Cu^{\delta+}]_n$ clusters), improves the structural regularity of the silicate. All of the materials exhibit high surface area and pore volume typical of the M41S type mesoporous structures. Moreover, a secondary mesoporosity was detected, which is likely caused by the hydrothermal treatment during the TIE process and may favor the diffusion and the exchange of the copper nano-species. TEM images show a primary mesoporous structure although there was no two-dimensional hexagonal ordering of pores characteristic of MCM-41 materials. On the other hand, unlike the DHT method, this new method would seem to disfavor the formation of large CuO particles. All of the samples show Lewis acid sites which result strong enough to retain the pyridine molecules until 200 °C. The two different synthesis methods analyzed, the DHT and TIE, result in different structure–property relationships of the Cu species incorporated to siliceous structure and consequently in different catalytic performance. The TIE method favors the dispersion of isolated $Cu^{\delta+}$ species on the mesopore wall, which are probably responsible for the higher cyclohexene conversion with H_2O_2 . The selectivity to allylic products was predominant which is giving account that

the reaction path involves the interaction of the Cu-MMS catalyst with peroxide which yields mainly $HO\cdot$ and $HO_2\cdot$ species via a redox mechanism.

Acknowledgments

G.A.E., K.S. and S.G.C are CONICET Researchers; C.M.Ch. and A.L.C received CONICET Doctoral Fellowship. This work was supported by CONICET, UTN-FRC and UNSL of Argentina, UMA of Spain, and UdeC of Chile. We thank to Dr. H. Thomas and Lic. N. Firpo (CINDECA, La Plata, Argentina) for DRUV-Vis data. Finally, C.M.Ch. acknowledge to Dra. M. E. Crivello for the participation in international cooperation project MINCYT-CONICYT, Code CH/08/03.

References

- [1] J.S. Beck, C.T. W. Chu, I.D. Johnson, C.T. Kresge, M.E. Leonowicz, W.J. Roth, J.W. Vartuli, Patent WO 91/11390 (1991).
- [2] C.T. Kresge, M.E. Leonowicz, W.J. Roth, J.W. Vartuli, J.S. Beck, *Nature* 359 (1992) 710–712.
- [3] J.S. Beck, J.C. Vartuli, W.J. Roth, M.E. Leonowicz, C.T. Kresge, K.D. Schmitt, C.T.W. Chu, D.H. Olson, E.W. Sheppard, S.B. McCullen, J.B. Higgins, J.L. Schlenker, *J. Am. Chem. Soc.* 114 (1992) 10834–10843.
- [4] J. Vartuli, K. Schmidt, C. Kresge, W. Roth, M. Leonowicz, S. McCullen, S. Hellring, J. Beck, J. Schlenker, D. Olson, E. Sheppard, *Chem. Mater.* 6 (1994) 2317–2326.
- [5] A. Corma, *Chem. Rev.* 97 (1997) 2373–2419.
- [6] J.M. Thomas, *Angew. Chem. Int. Ed. Engl.* 38 (1999) 3588–3628.
- [7] G. Soler-Illia, C. Sanchez, V. Lebeau, J. Patarin, *Chem. Rev.* 102 (2002) 4093–4138.
- [8] D. Loy, V. Shea, *Chem. Rev.* 95 (1995) 1431–1442.
- [9] M. Yonemitsu, Y. Tanaka, M. Iwamoto, *Chem. Mater.* 9 (1997) 2679–2681.
- [10] M. Yonemitsu, Y. Tanaka, M. Iwamoto, *J. Catal.* 178 (1998) 207–213.
- [11] C. Liu, H. Teng, *Appl. Catal. B: Environ.* 58 (2005) 69–77.
- [12] Q. Zhang, Y. Wang, Y. Ohishi, T. Shishido, K. Takehira, *J. Catal.* 202 (2001) 308–318.
- [13] Q. Zhang, Y. Wang, Y. Ohishi, T. Shishido, K. Takehira, *Chem. Lett.* (2001) 194–195.
- [14] Y. Wang, Q. Zhang, Y. Ohishi, T. Shishido, K. Takehira, *Catal. Lett.* 72 (2001) 215–219.
- [15] Q. Zhang, W. Yang, X. Wang, Y. Wang, T. Shishido, K. Takehira, *Microporous Mesoporous Mater.* 77 (2005) 223–234.
- [16] Y. Wang, Q. Zhang, T. Shishido, K. Takehira, *J. Catal.* 209 (2002) 186–196.
- [17] Q. Zhang, Y. Wang, S. Itsuki, T. Shishido, K. Takehira, *Chem. Lett.* (2001) 946–947.
- [18] Y. Wang, Y. Ohishi, T. Shishido, Q. Zhang, W. Yang, Q. Guo, H. Wan, K. Takehira, *J. Catal.* 220 (2003) 347–357.
- [19] Q. Zhang, Y. Wang, S. Itsuki, T. Shishido, K. Takehira, *J. Mol. Catal. A* 188 (2002) 189–200.
- [20] K. Ikeda, Y. Kawamura, T. Yamamoto, M. Iwamoto, *Catal. Commun.* 9 (2008) 106–110.
- [21] W. Sanderson, *Pure Appl. Chem.* 72 (2000) 1289–1304.
- [22] G.A. Eimer, S.G. Casuscelli, G.E. Ghione, M.E. Crivello, E.R. Herrero, *Appl. Catal. A* 298 (2006) 232–242.
- [23] C.M. Chanquía, A.L. Cánepa, K. Sapag, P. Reyes, S.G. Casuscelli, E.R. Herrero, G.A. Eimer, *Topics Catal.* 54 (2011) 160–169.
- [24] P. Selman, S.E. Dapurkar, *J. Catal.* 229 (2005) 64–77.
- [25] B. Chou, J.L. Tsai, S. Cheng, *Microporous Mesoporous Mater.* 48 (2001) 309–317.
- [26] X.Y. Hao, Y.Q. Zhang, J.W. Wang, W. Zhou, C. Zhang, S. Liu, *Microporous Mesoporous Mater.* 88 (2005) 38–47.
- [27] Y. Kobayashi, S. Ishida, K. Ihara, Y. Yasuda, T. Morita, S. Yamada, *Colloid Polym. Sci.* 287 (2009) 877–880.
- [28] M. Ghadiri, F. Farzaneh, M. Ghandi, M. Alizadeh, *J. Mol. Catal. A* 233 (2005) 127–131.
- [29] G.A. Eimer, S.G. Casuscelli, C.M. Chanquía, V.R. Elías, M.E. Crivello, E.R. Herrero, *Catal. Today* 133–135 (2008) 639–646.
- [30] V. Elías, M. Oliva, S. Urreta, S. Silveti, K. Sapag, A. Mudarra Navarro, S. Casuscelli, G. Eimer, *Appl. Catal. A* 381 (2010) 92–100.
- [31] N. Malumbazo, S.F. Mapolie, *J. Mol. Catal. A* 312 (2009) 70–77.
- [32] C.M. Chanquía, K. Sapag, E. Rodríguez-Castellón, E.R. Herrero, G.A. Eimer, *J. Phys. Chem. C* 114 (2010) 1481–1490.
- [33] C.M. Chanquía, L. Andrini, J.D. Fernández, M.E. Crivello, F.G. Requejo, E.R. Herrero, G.A. Eimer, *J. Phys. Chem. C* 114 (2010) 12221–12229.
- [34] W. Gac, A. Derylo-Marczewska, S. Pasieczna-Patkowska, N. Popivnyak, G. Zukocinski, *J. Mol. Catal. A* 268 (2007) 15–23.
- [35] H.T. Gomes, P. Selvam, S.E. Dapurkar, J.L. Figueiredo, J.L. Faria, *Microporous Mesoporous Mater.* 86 (2005) 287–294.
- [36] A. Gervasini, S. Bennici, *Appl. Catal. A* 281 (2005) 199–205.
- [37] T. Tsoncheva, T. Venkov, M. Dimitrov, C. Minchev, K. Hadjiivanov, *J. Mol. Catal. A* 209 (2004) 125–134.

- [38] J. Okamura, S. Nishiyama, S. Tsuruya, M. Masai, *J. Mol. Catal. A* 135 (1998) 133–142.
- [39] Q. Wu, X. Hu, P.L. Yue, X.S. Zhao, G.K. Lu, *Appl. Catal. B* 32 (2001) 151–156.
- [40] A.L. Patterson, *Phys. Rev.* 56 (1939) 978–982.
- [41] K.S.W. Sing, D.H. Everett, R.A.W. Haul, L. Moscou, R.A. Pierotti, J. Rouquerol, T. Siemieniowska, *Pure Appl. Chem.* 57 (1985) 603–619.
- [42] M. Kruk, M. Jaroniec, R. Ryoo, J.M. Kim, *Chem. Mater.* 11 (1999) 2568–2572.
- [43] M. Kruk, M. Jaroniec, Y. Sakamoto, O. Terasaki, R. Ryoo, C. Hyun ko, *J. Phys. Chem. B* 104 (2000) 292–301.
- [44] I. Díaz, J. Pérez-Pariente, *Chem. Mater.* 14 (2002) 4641–4646.
- [45] F. Rouquerol, J. Rouquerol, K. Sing, *Adsorption by Powders and Porous Solids. Principles, Methodology and Applications*, Academic Press, London, 1999.
- [46] X. Liu, H. Sun, Y. Chen, Y. Yang, A. Borgna, *Microporous Mesoporous Mater.* 121 (2009) 73–78.
- [47] J. Agúndez, *Stud. Surf. Sci. Catal.* 154 (2004) 2907–2914.
- [48] M. Occelli, S. Biz, A. Auroux, *Appl. Catal. A* 183 (1999) 231–239.
- [49] F. Kleits, W. Schmidt, F. Schüth, *Microporous Mesoporous Mater.* 44–45 (2001) 95–109.
- [50] H. Pralialud, Z. Chajar, M. Primet, *Appl. Catal. B* 16 (1998) 359–374.
- [51] M.C.N.A. De Carvalho, F.B. Passos, M. Schmal, *Appl. Catal. A* 193 (2000) 265–276.
- [52] Y. Jiang, Q. Gao, *Mater. Lett.* 61 (2007) 2212–2216.
- [53] Z.R. Ismagilov, S.A. Yashnik, V.F. Anufrienko, T.V. Larina, N.T. Vasenin, N.N. Bulgakov, S.V. Vosek, L.T. Tsykoza, *Appl. Surf. Sci.* 226 (2004) 88–93.
- [54] S.A. Yashnik, Z.R. Ismagilov, V.F. Anufrienko, *Catal. Today* 110 (2005) 310–322.
- [55] V.F. Anufrienko, N.N. Bulgakov, N.T. Vasenin, S.A. Yashnik, L.T. Tsikoza, S.V. Vosek, Z.R. Ismagilov, *Dokl. Akad. Nauk* 386 (2002) 770.
- [56] V.F. Anufrienko, S.A. Yashnik, N.N. Bulgakov, T.V. Larina, N.T. Vasenin, Z.R. Ismagilov, *Dokl. Akad. Nauk* 392 (2003) 67–71.
- [57] V.F. Anufrienko, S.A. Yashnik, N.N. Bulgakov, T.V. Larina, N.T. Vasenin, Z.R. Ismagilov, *Dokl. Phys. Chem.* 392 (2003) 207–211.
- [58] S. Velu, K. Suzuki, M. Okazaki, M.P. Kapoor, T. Osaki, F. Ohashi, *J. Catal.* 194 (2000) 373–384.
- [59] L. Chmielarz, P. Kustrowski, R. Dziembaj, P. Cool, E.F. Vansant, *Appl. Catal. B* 62 (2006) 369–380.
- [60] M. Santhosh Kumar, M. Schwidder, W. Grünert, A. Brückner, *J. Catal.* 227 (2004) 384–397.
- [61] Y. Wan, J. Ma, Z. Wang, W. Zhou, S. Kaliaguine, *Appl. Catal. B* 59 (2005) 235–242.
- [62] A.J. Marchi, D.A. Gordo, A.F. Trasarti, C.R. Apesteguía, *Appl. Catal. A* 249 (2003) 53–67.
- [63] S. Velu, L. Wang, M. Okazaki, K. Suzuki, S. Tomura, *Microporous Mesoporous Mater.* 54 (2002) 113–126.
- [64] M.C.N.A. De Carvalho, F.B. Passos, M. Schma, *Appl. Catal. A* 193 (2000) 265–276.
- [65] S. Bennici, A. Gervasini, N. Ravasio, F. Zaccheria, *J. Phys. Chem. B* 107 (2003) 5168–5176.
- [66] J.P. Espinos, J. Morales, A. Barranco, A. Caballero, J.P. Holgado, A.R. Gonzalez-Eliphe, *J. Phys. Chem. B* 106 (2002) 6921–6929.
- [67] I. Jirka, V. Bosacek, *Zeolites* 11 (1991) 77–80.
- [68] G. Avgouropoulos, T. Ioannides, *Appl. Catal. A* 244 (2003) 155–167.
- [69] J.M. Lazaro, E. Rodríguez-Castellón, *J. Mol. Catal.* 339 (2011) 43–51.
- [70] U.G. Singh, R.T. Williams, K.R. Hallam, G.C. Allen, *J. Solid State Chem.* 178 (2005) 3405–3413.
- [71] D. Trong On, S. Nguyen, V. Hulea, E. Dumitriu, S. Kaliaguine, *Microporous Mesoporous Mater.* 57 (2003) 169–180.
- [72] D. Srinivas, R. Srivastava, P. Ratnasamy, *Catal. Today* 96 (2004) 127–133.
- [73] B. Chakraborty, B. Viswanathan, *Catal. Today* 49 (1999) 253–260.
- [74] A. Sakthivel, S. Dapurkar, N. Gupta, S. Kulshreshtha, S. Selvam, *Microporous Mesoporous Mater.* 65 (2003) 177–187.
- [75] T. Conesa, J. Hidalgo, R. Luque, J. Campelo, A. Romero, *Appl. Catal. A* 299 (2006) 224–234.
- [76] C. Otero Areán, M. Rodríguez Delgado, V. Montouillout, J. Lavalley, C. Fernández, J. Cuart Pascual, J. Parra, *Microporous Mesoporous Mater.* 67 (2004) 259–264.
- [77] L. Cedeño, D. Hernández, T. Klimova, J. Ramírez, *Appl. Catal. A* 241 (2003) 39–50.
- [78] E. Escalona Platero, M. Peñarroya Mentruit, C. Otero Areán, A. Zecchina, *J. Catal.* 162 (1996) 268–276.
- [79] C. Morterra, G. Magnacca, *Catal. Today* 27 (1996) 497–532.
- [80] L. Chen, L. Noreña, J. Navarrete, J. Wang, *Mater. Chem. Phys.* 97 (2006) 236–242.
- [81] F. Gao, Y. Zhang, H. Wan, Y. Kong, X. Wu, L. Dong, B. Li, Y. Chen, *Microporous Mesoporous Mater.* 110 (2008) 508–516.
- [82] Y. Segura, P. Cool, P.P. Kustroeski, L. Chmielarz, R. Dziembaj, E.F. Vansant, *J. Phys. Chem. B* 109 (2005) 12071.
- [83] X.Y. Hao, Y.Q. Zhang, J. Wang, W. Zhou, C. Zhang, S. Liu, *Microporous Mesoporous Mater.* 88 (2005) 38–47.
- [84] M. Anpo, M. Matsuoka, Y. Shioya, H. Yamashita, E. Giamello, C. Monterra, M. Che, H.H. Patterson, S. Webber, S. Ouellette, M.A. Fox, *J. Phys. Chem.* 98 (1994) 5744–5750.
- [85] I.V. Babich, Y.V. Plyuto, P. Van der Voort, E.F. Vansant, *J. Colloid Interface Sci.* 189 (1997) 144–150.
- [86] L. Noreña-Franco, I. Hernandez-Perez, J. Aguilar-Pliego, A. Maubert-Franco, *Catal. Today* 75 (2002) 189–195.
- [87] J. Martinez, M. Leal Denis, L. Piehl, E. Celis, G. Buldain, V. Campo DalÍOrto, *Appl. Catal. B* 82 (2008) 273–283.
- [88] V. Hulea, E. Dumitriu, F. Patcas, R. Ropot, P. Graffin, P. Moreau, *Appl. Catal. A* 170 (2008) 169–175.
- [89] I. Nowak, B. Kilos, M. Ziolk, A. Lewandowska, *Catal. Today* 78 (2003) 487–498.
- [90] S.G. Casuscelli, G.A. Eimer, A. Canepa, A.C. Heredia, C.E. Poncio, M.E. Crivello, C.F. Perez, A. Aguilar, E.R. Herrero, *Catal. Today* 133–135 (2008) 678–683.
- [91] M. Salavati-Niasari, F. Farzaneh, M. Ghandi, *J. Mol. Catal. A* 186 (2002) 101–107.
- [92] R.S. Disselkamp, B.D. Harris, J.N. Patel, T.R. Hart, C.H.F. Peden, *Inorg. Chem. Commun.* 11 (2008) 561–563.
- [93] G.A. Eimer, I. Díaz, E. Sastre, S.G. Casuscelli, M.E. Crivello, E.R. Herrero, J. Perez-Pariente, *Appl. Catal. A* 343 (2008) 77–86.
- [94] Y. Suh, N. Kim, W. Ahn, H. Ree, *J. Mol. Catal. A: Chem.* 174 (2001) 249–254.
- [95] W. Hölderich, J. Röseler, G. Heitmann, A. Liebens, *Catal. Today* 37 (1997) 353–366.
- [96] R.A. Sheldon, J.A. Kochi, *Metal-Catalyzed Oxidations of Organic Compounds*, Academic Press, New York, 1981.
- [97] L. Garrel, M. Bonetti, L. Tonucci, M. Bressan, *J. Photochem. Photobiol. A* 179 (2006) 193–199.
- [98] S. Sato, R. Takahashi, H. Fukuda, K. Inui, *J. Mol. Catal. A* 272 (2007) 164–168.